Simulating Hypersonic Magnetofluid-Dynamic Compression in Rectangular Inlet

J. S. Shang*
Wright State University, Dayton, Ohio 45435
C. L. Chang[†]
NASA Langley Research Center, Hampton, Virginia 23681
and
S. T. Surzhikov[‡]
Russian Academy of Sciences, 119526, Moscow, Russia

The combined effects of an electromagnetic perturbation and viscous–inviscid interaction generate a high-pressure plateau near the hypersonic leading edge surface. The surface pressure induced by magnetofluid-dynamic interaction emulates a movable leading edge strake. This phenomenon has been verified in experimental research, which shows that a direct current surface discharge becomes a virtual compression ramp for flow control. More recently, investigation has extended to a rectangular hypersonic inlet. The present analysis solves the magnetofluid-dynamic equations using weakly ionized gas models, including the formulation based on the drift–diffusion theory. The numerical simulation provides a detailed description of the intriguing magnetofluid-dynamic interacting flowfield. After validation by experimental measurements, the computed results quantify the effectiveness of a magnetofluid-dynamic compression for a hypersonic inlet. Applying a plasma generation power input to a direct current surface discharge of 7.87 W per square centimeter of electrode area, the interaction produces an 11.7% higher compression of a constant cross-section inlet.

Nomenclature

B	=	magnetic flux density
E	=	electrical field strength
F	=	flux vector of the magnetofluid-dynamic equations
J	=	electric current density
n_e, n_+	=	number density of charged particles
P	=	pressure
Q	=	dependent variable vector
u	=	velocity vector
α	=	Townsend's ionization coefficient
β	=	recombination coefficient
Γ_e, Γ_+	=	flux density of charged particles
ρ	=	density
τ	=	shear stress tensor
φ	=	electric potential

I. Introduction

THE viscous–inviscid flow interaction within the inlet of a high-speed propulsive system remains one of the most challenging topics in aerodynamics [1,2]. Formidable difficulties arise from the nonlinear phenomena associated with widely varying temporal and length scales, the laminar-turbulent transition, and turbulent motion [3–5]. In addition, the propulsion requirement in high-speed flights varies greatly and cannot be supported by a fixed inlet configuration. However once a variable configuration inlet is implemented by an array of compression ramps and boundary-layer control slots, a complicated mechanical flow control system must be adopted to eliminate parasitic effects when operating beyond the design condition. For this reason, an alternative, nonintrusive, rapid response flow control mechanism by other than mechanical means should be very appealing.

Resler and Sears [6] advocated flow control using plasma as early as the late 1950s. The most attractive aspect of their ideas is the introduction of electromagnetic forces beyond traditional aerodynamics for flowfield manipulation. More recently, Chernyi [7] has provided an interesting assessment of magnetohydrodynamic applications for high-speed flow control. Bityurin et al. [8] also performed extensive experimental studies of the effects of heterogeneous plasma on the structure and propagation of shock waves. Most recently, Lennov et al. [6] have investigated the basic mechanism of plasma and aerodynamic interaction near solid surfaces. Innovative ideas have also been put forward for hypersonic flow control, including thrust vectoring, with and without the presence of an externally applied magnetic field [7–10].

Numerous concepts have also been put forward for using electromagnetic force for high-speed flow control [11–20]. Some of the research efforts include an externally applied magnetic field that attempts to accentuate the magnetofluid-dynamic (MFD) interaction by invoking the Lorentz force in addition to Joule heating [12,13,15–17,19,20]. Surzhikov and Shang [21,22] have shown that the Hall effect exerts significant influence on plasma generation via the electron collision process. The Hall current effect can also suppress the MFD interaction when the value of the Hall parameter is exceedingly high. However with a relatively weak applied magnetic field, $B \leq 0.2$ T, the interaction is enhanced by the presence of an externally applied magnetic field. This finding is supported by experimental efforts by Menart et al. [12] and Kimmel et al. [13]. In a numerical simulation around a cone in hypersonic flow, Borghi et al. [20] also finds that the Hall current can significantly weaken the

*Research Professor, Department of Mechanics and Materials Engineering; joseph.shang@wright.edu. Fellow AIAA.
[†]Research Scientist, Computational Aerosciences Branch. Associate Fellow AIAA.
[‡]Professor, Institute for Problems in Mechanics. Associate Fellow AIAA.

MFD interaction. All the aforementioned computing simulations are in general agreement with the experimental observations of Bityurin et al. [14] on the effect of Hall current in MFD interactions.

To study the effect of an electromagnetic perturbation on a hypersonic viscous–inviscid interaction for flow control without any ambiguity, the present approach must demonstrate a direct link of cause and consequence. The most obvious choice is in the sharp leading edge domain, where the flow is laminar and the intensity of the perturbation can be relatively weak but can exert a profound influence on the entire flowfield. The classic hypersonic flow theory by Hayes and Probstein [23] describes the viscous–inviscid interaction over a sharp leading edge as the pressure interaction. The pressure distribution near the leading edge of a solid surface can be substantially altered by the growth rate of the displacement thickness of the boundary layer. The outward deflected streamlines induce a high-pressure region that will extend far downstream for flow modification. The magnitude of the induced pressure is well known and can be calculated by a single interaction parameter: $\chi = M^3(C/\text{Rey})^{1/2}$. The viscous–inviscid interaction is strongly amplified in hypersonic flows because of its cube power dependence on the Mach number. Several experimental and computational investigations have focused on exploiting this property by introducing the electromagnetic effect for flow control [12,13,15,16]. This control mechanism can actuate in microseconds and induces a higher surface pressure, mimicking a deflected leading edge strake. Results from both experimental and computational efforts have shown the chain of events that can be initiated by an electromagnetic perturbation and amplified by viscous–inviscid interactions to constitute a very effective hypersonic flow control technique. The triggering mechanism is a simple direct current surface discharge [15].

This concept has been fully validated as an MFD flow control mechanism through side-by-side experimental and computational investigations [15,16]. Most recently, following this train of thought, experimental research has shown the amplified viscous–inviscid interaction near the leading edge of a constant cross-section rectangular inlet acting as a virtual variable geometry cowl [24,25]. A simple direct current glow discharge generates from a pair of embedded electrodes on the sidewalls, introducing an electromagnetic perturbation. This perturbation is subsequently amplified by the viscous–inviscid interaction to produce a compression downstream of the inlet. In the experimental effort only Pitot pressure surveys were collected, but the data indicated promising potential. This repeatable MFD interaction is equivalent to MFD sidewall compressions for practical applications.

In the present approach, a numerical simulation duplicates the experiment to complete the side-by-side investigation of the rather complex MFD interaction. The partially ionized air models, ranging from a simple phenomenological approximation to the rigorous drift–diffusion theory, are used to describe the nonequilibrium dc discharge [16,17,21,22]. The electrodes of the dc discharge are embedded in the sidewalls of a constant cross-section area inlet; this arrangement is nonintrusive when deactivated. Once the discharge is actuated, the combined volumetric Joule and conductive electrode heating increases the local displacement thickness. The increased slope of the displacement thickness generates a series of compression waves and coalesces into an oblique shock through an aerodynamic viscous–inviscid interaction. The compression is directly controlled by the power input of the electromagnetic perturbation. Furthermore, at a higher freestream Mach number, it automatically generates a greater compression through the stronger viscous–inviscid interaction.

The classic MFD equations in the low magnetic Reynolds number limit, which duplicate the previous experimental conditions, are solved to generate the numerical simulations [25]. The numerical solutions are first calibrated with the measured Pitot pressure surveys, and then the critical aerodynamic parameters of the inlet performance are evaluated. The Mach number profiles, the stagnation pressure, and the static pressure distributions are presented to describe the overall flowfield structure of the MFD compression inlet.

II.   Governing Equations

In most aerodynamic applications of flow control using a plasma actuator, the magnetic Reynolds number is much less than unity, $Re_m = \mu\sigma u L \ll 1$ [26,27]. According to the investigated flow condition, Re_m has a value of 8.48×10^{-6}; thus the governing equations of the low magnetic Reynolds number approximation are fully justified for the present investigation [26]:

$$\partial\rho/\partial t + \nabla \cdot (\rho \boldsymbol{u}) = 0 \tag{1}$$

$$\partial\rho\boldsymbol{u}/\partial t + \nabla \cdot (\rho\boldsymbol{uu} - \tau) = \mathbf{J} \times \mathbf{B} \tag{2}$$

$$\partial\rho e/\partial t + \nabla \cdot (\rho e\boldsymbol{u} - \mathbf{q} - \boldsymbol{u} \cdot \tau) = \mathbf{E} \cdot \mathbf{J} \tag{3}$$

The electrostatic force term $\rho_e \cdot \mathbf{E}$ is omitted in the traditional formulation. This simplification is easily seen in a simple order-of-magnitude analysis. In an airstream that flows at a velocity of up to 10^5 m/s with a linear varying electric field, the ratio of the transport of excess charges to the conducting electric current $(\rho_e \boldsymbol{u})/(\sigma \mathbf{E})$ has a value of 10^{-8} [27]. In the present investigation, the applied electric field intensity is limited to a value less than 1 kV; the magnitude of the electrostatic force is merely a few dynes per cubic centimeter [28,29].

The governing partial differential equation system is identical to the Navier–Stokes equations except for the nonzero source terms. The dc discharge has the maximum positive charged particle number density in the cathode layer, which has been measured to be about 8.8×10^{11}/cc, and the electrical conductivity is less than 1 mho/m locally. At the experimental stagnation pressure of 580 torr, the air number density is 1.57×10^{17}/cc; thus the mass fraction of the charged particles is 10^{-6}. It is therefore reasonable to consider only the transport properties of the weakly ionized air and to neglect the effects of the nonequilibrium thermodynamics and chemical kinetics.

The electromagnetic perturbation enters the MFD interaction as volumetric Joule heating and convective electrode heat transfer from the solid boundary. These two fundamentally different heat transfer processes occur on vastly different time scales; the former takes place the instant the plasma is ignited, on the order of microseconds, and the heat source is confined to a few Debye lengths immediately adjacent to the electrodes [26,27,30]. The convective heat transfer, on the other hand, will not reach an equilibrium state within the time frame of the tests [12,13]. The heating effects thicken the displacement thickness of the shear layer on the inlet surface, and they are cumulative. To describe this perturbation for as wide a range of weakly ionized models as possible, the total amount of energy released into the airstream is calculated from a partially ionized plasma model based on the drift–diffusion theory [30]. Surzhikov and Shang [22] have successfully developed a model of a three-component plasma (neutral, electron, and ion) and two-temperature plasma:

$$\partial n_e/\partial t + \nabla \cdot \Gamma_e = \alpha(E, p)|\Gamma_e| - \beta n_+ n_e \tag{4}$$

$$\partial n_+/\partial t + \nabla \cdot \Gamma_+ = \alpha(E, p)|\Gamma_e| - \beta n_+ n_e \tag{5}$$

$$\Gamma_e = -D_e \nabla n_e - n_e \mu_e \mathbf{E} \tag{6}$$

$$\Gamma_+ = -D_+ \nabla n_+ + n_+ \mu_+ \mathbf{E} \tag{7}$$

In the above formulation, $\alpha(E, p)$ and β are the first Townsend ionization coefficient and recombination coefficient, μ_e and μ_+ are the electron and ion mobility, and D_e and D_+ are the electron and ion diffusion coefficients [30]. The electrical current density appears in the low magnetic Reynolds number approximation and is computed using

$$\mathbf{J} = e(\Gamma_+ - \Gamma_e) \tag{8}$$

A compatible electrical field intensity $\mathbf{E}$ of the discharge domain is obtained by satisfying the charge conservation equation [15,16]. This equation can be further simplified in a globally neutral plasma by introducing an electrical potential function $\mathbf{E} = -\nabla\phi$. The electric potential is then the solution of the well-known Poisson equation of plasma dynamics associated with a net space charge density ρ_e [26,27]:

$$\nabla^2\phi = -\rho_e/\varepsilon \tag{9}$$

The initial values and boundary conditions, as well as the numerical procedure, are directly usable from the accumulated knowledge from the CFD discipline [15–19]. For the velocity components, the freestream and no-change conditions are prescribed at the entrance, far field, and exit boundaries of the computational domain, respectively. The no-slip condition applies to all the velocity components on the inlet solid surface. The adiabatic condition is used to determine the surface gas temperature on the inlet surface. Finally the surface density is evaluated locally by the vanishing normal pressure gradient condition.

The initial values and boundary conditions of the plasma model for a numerically stable procedure have been found through a series of sustained research efforts [15,16,21,22]. A key element in determining the boundary conditions is specifying the electron number density on the cathode for the secondary emission phenomenon. This physical requirement is met by requiring the normal component of the electron flux at the cathode to be proportional to the ion counterpart:

$$\Gamma_e \cdot \mathbf{n} = -\gamma\Gamma_+ \cdot \mathbf{n} \tag{10}$$

where γ is the secondary emission coefficient and $\mathbf{n}$ is the unit outward normal vector of the solid surface. This coefficient depends on the material of the cathode and intensity of the electrical field. Raizer [30] has extensively studied the influence of γ on the structure of the gas discharge. For direct current discharges in nitrogen, a value from 0.01 to 0.1 is recommended. A range of secondary emission coefficients for dc discharge has been used in a large group of numerical simulations [15–18,21,22]. Values of γ from 0.1 to 0.3 actually improve the computation stability, and the agreement between computed results and experimental data also justifies their adoption.

III. Numerical Procedure

All numerical results are obtained by solving the time-dependent governing equations in conservative variables. The spatial discretization is based on a semidiscrete finite-volume scheme [31]. The upwind-biasing approximation is applied to the convective and pressure terms, and central differencing is used for the shear stress and heat transfer terms.

In the flux-difference splitting procedure, the flux vectors at the control surface are written as an exact solution to the approximate Riemann problem:

$$(\delta F)_i = \tfrac{1}{2}[F(\mathbf{Q}_L) + F(\mathbf{Q}_R)] - |\mathbf{M}_{\text{inv}}|(\mathbf{Q}_R - \mathbf{Q}_L)]_{i+1/2} - \tfrac{1}{2}[F(\mathbf{Q}_L)$$
$$+ F(\mathbf{Q}_R)] - |\mathbf{M}_{\text{inv}}|(\mathbf{Q}_R - \mathbf{Q}_L)]_{i-1/2} \tag{11}$$

where $\mathbf{Q}_L$ and $\mathbf{Q}_R$ are the interpolated values of dependent variables, ρ, ρu, ρv, ρw, and ρe, on the interface of the control volume. $\mathbf{M}_{\text{inv}}$ is the Jacobian matrix of the inviscid or convective terms, $\mathbf{M}_{\text{inv}} = \partial F_{\text{inv}}/\partial \mathbf{Q}$ [31].

The time advancement is implicit to solve the flows with a steady asymptote. A slope limiter is also used to control the discontinuous pressure jumps at the shock front. Specifically the min–mod limiter is adopted for the present computations:

$$(\mathbf{Q}_L)_{i+1/2} = \mathbf{Q}_i + \tfrac{1}{4}[(1 - \kappa)\Delta_- + (1 + \kappa)\Delta_+]_i \tag{12}$$

$$(\mathbf{Q}_R)_{i+1/2} = \mathbf{Q}_{i+1} - \tfrac{1}{4}[(1 - \kappa)\Delta_+ + (1 + \kappa)\Delta_-]_{i+1} \tag{13}$$

The one-sided difference operators are $\Delta_+ = \mathbf{Q}_{i+1} - \mathbf{Q}_i$ and $\Delta_- = \mathbf{Q}_i - \mathbf{Q}_{i-1}$, and the min–mod operators are defined as

$$\Delta_- = \min \text{mod}[\Delta_-, (3 - \kappa)/(1 - \kappa)\Delta_+] \tag{14}$$

$$\Delta_+ = \min \text{mod}[\Delta_+, (3 - \kappa)/(1 - \kappa)\Delta_-] \tag{15}$$

All numerical results replicate the flow conditions of an earlier experimental investigation in a hypersonic inlet [25]. The rectangular inlet model has dimensions of $10.1 \times 3.81 \times 3.11$ cm. At a fixed stagnation temperature of 270 K and an unperturbed freestream Mach number of 5.15, the static temperature of the free jet is 43 K, and it has a freestream velocity of 675.5 m/s. To ensure a stable inflow environment, tests were conducted at two stagnation pressures of 370 and 580 torr. The incoming airstreams therefore have static pressures of 0.59 or 0.92 torr (78.4 or 122.2 Pa) and densities of 6.4×10^{-3} or 10.03×10^{-3} kg/m^3 according to the different stagnation pressures. These conditions produce two Reynolds numbers based on the model lengths of 1.64×10^5 and 2.57×10^5, respectively. At the hypersonic Mach number and the relatively low Reynolds numbers, the flow fields are considered to be laminar.

The incoming flow is along the x coordinate, and the freestream condition is prescribed on the four clustered and consecutive crossflow planes upstream to the leading edge of the inlet. Then, the streamwise grid space is stretched from there toward downstream. The finest grid spacing is located immediately adjacent and normal to the walls and is one-hundredth of the boundary-layer thickness in size at the inlet exit. The mesh space in the crossflow planes is geometrically stretched from the wall surface to the centerline of the inlet by a constant value of 1.05. Invoking the symmetric condition with respect to the y coordinate, the total number of grid points in the computational domain is reduced by one-half. Two mesh systems are used for numerical resolution assessment: the coarse and fine-mesh systems consist of ($85 \times 45 \times 81$) and ($105 \times 57 \times 101$) in the x, y, and z coordinates, respectively. The solutions of the two mesh systems differ by a maximum of less than 6% for the calculated Pitot pressure. For this reason, most of the presented numerical results are derived from the fine-mesh calculations.

To accelerate convergence, three-level mesh sequencing of the multigrid technique is adopted [32]. The mesh systems of the half ($41 \times 23 \times 43$) and quarter ($21 \times 12 \times 22$) mesh number densities are used for the coarse mesh computations. The data processing rate on a 400 mHz SGI Octane2 workstation is 61.6×10^{-6} s per number of cells per number of iterations. The convergence criterion of the present analysis is preset at a value of 3.0×10^{-7} of the normalized global residue for the finite-volume scheme. The characteristic behavior of iterative convergence is presented in Fig. 1. It is clearly seen that the solution has attained its steady state asymptote after 300 iterations. A typical calculation requires around 5400 s to reach its steady asymptote.

IV. Unperturbed Flowfield Structure

A geometrically simple rectangular inlet possesses a rather complex shock wave structure within the hypersonic inlet. Four oblique shocks emanate from the mutually perpendicular leading edges of the rectangular inlet. The height of the inlet is slightly greater than the width of the inlet (3.81 vs 3.11 cm). Therefore two shock waves that originate from the leading edge parallel to the z coordinate intercept upstream of the shocks parallel to the y coordinate. The pressure contours of the induced oblique shock waves from the leading edges of the sidewalls on the centerline of the x–y plane are depicted in Fig. 2. This figure displays the oblique shocks emanating from the leading edges and intersecting each other before leaving the exit plane. Coalescing and interacting compression waves are also visible upstream of the shock
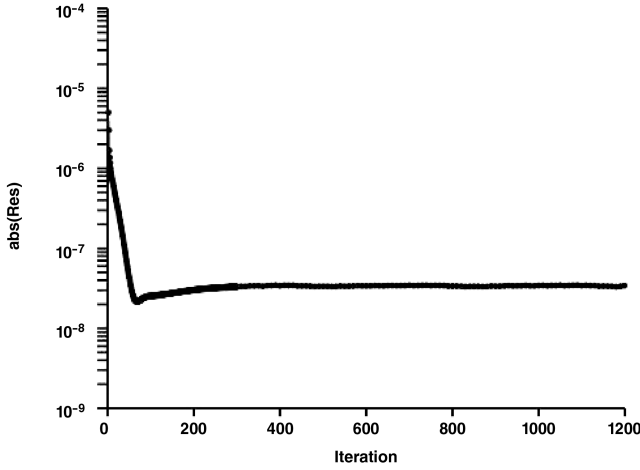
Fig. 1   Convergence characteristic of multigrid solution.

intersection points. Nearly identical wave structures also exist in the x–z plane. Therefore there are at least four oblique shocks that coexist in the crossflow plane. In short, complex shock–shock and shock-boundary interactions are occurring within this simple inlet.

In Fig. 3, an intriguing flowfield structure is revealed by the selected Mach number contours at three streamwise locations. These numerical results were generated using the fine-mesh system. Upstream of the intersection of the four equal strength oblique shocks, a connecting shock wave must exist between two perpendicular families of shocks to satisfy the continuity condition [33]. At the intersection of the oblique and the connecting shocks, two triplet points are formed. Therefore a total of eight triplet points are contained in the shock formation of each cross-sectional plane ($x/L = 0.25$). Beneath the connection shock, the compression is stronger than from a single oblique shock; thus, the viscous layer approaching the corner region is thinner than that on the sidewall. In the next two cross-sectional planes, the four oblique shocks are seen to intersect and diverge from each other toward the exit plane. Because the width is smaller than the height of the inlet, oblique

shocks emanating from the leading edge parallel to the z coordinate intersect first and then divert from each other downstream. At the exit plane, the viscous dissipation and wave attenuation eventually blend the Mach number distribution into a nearly uniform distribution from the four distinct weak shocks.

The complicated shock–shock interaction of the shocks of equal strength can be better appreciated in the density contours. Figure 4 shows the top view and side view of the density contours on the central plane of the inlet. In this presentation, the four interacting shocks are displayed. The shocks originating from the leading edge parallel to the z coordinate intersect first and across the entire width of the x–y plane at $x/L = 0.475$. Meanwhile, the shocks perpendicular to them intersect at a downstream location, $x/L = 0.54$. The density distribution also reveals a weak viscous–inviscid interaction at the leading edge of the inlet.

V.   Computed Results Validation

In the preliminary study, the cathode and anode are embedded in opposite sidewalls parallel to the z coordinate. However most experimental data are collected for the arrangement of electrodes where the cathode and anode are embedded in each side of the vertical sidewalls. The four electrodes have identical dimensions ($3.175 \times 0.64 \times 0.16$ cm, length × width × depth). The cathodes are placed at a short distance of 0.64 cm downstream of the leading edge, and the distance between the centerline of the cathode and anode is 2.22 cm.

Figure 5 presents the photographic top view of the flowfield within the inlet with the actuating dc discharge along the sidewalls. The discharge is generated by an electrical field intensity from 600 to 800 V and an electric current range from 40 to 80 mA [25]. At the total discharge surface area of 8.13 cm^2, the minimum discharge current density is around 13.3 mA/cm^2; thus for either circumstance the discharge is in the abnormal glow regime. When the dc discharge is activated in the plasma channel, flowfield fluctuations over wide spectra are detected [25]. Nevertheless the electromagnetic field is introduced into the flowfield as a small perturbation; the basic flow structure is unaltered. The only changes are reflected by the stronger oblique shock waves. This modification is detectable by the steeper
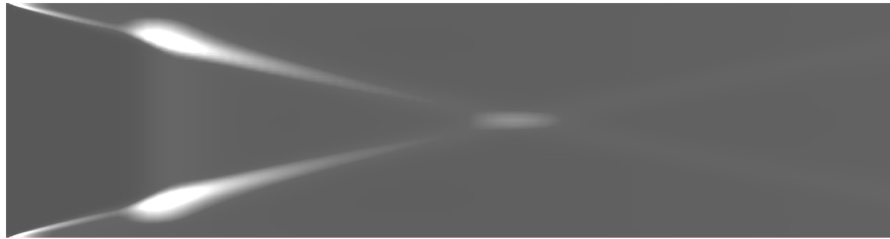

Fig. 2   Shockwave structure in the x–y plane, $M_\infty = 5.15$, Rey $= 1.64 \times 10^5$ ($105 \times 101 \times 57$).
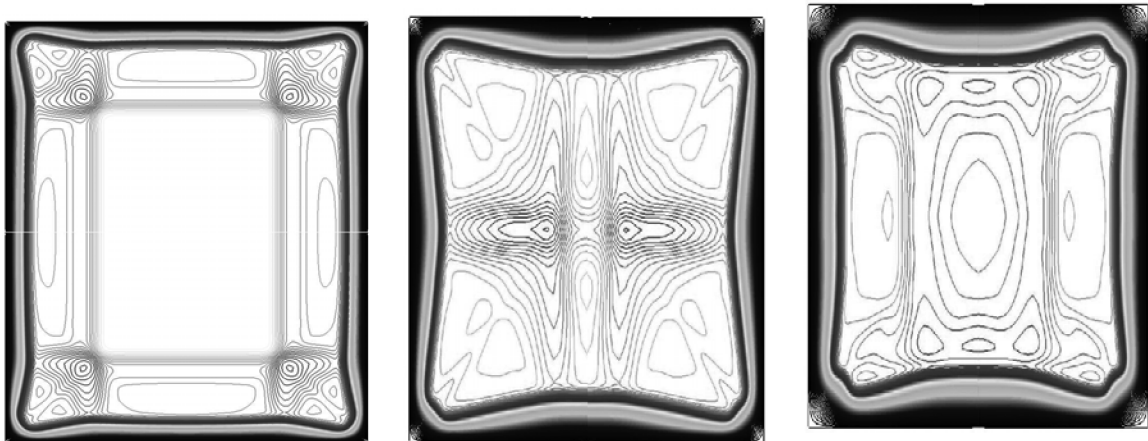

Fig. 3   Mach number contours at three streamwise cross sections, $x/L = 0.25$, 0.56, and 1.0, $M_\infty = 5.15$, Rey $= 1.64 \times 10^5$.
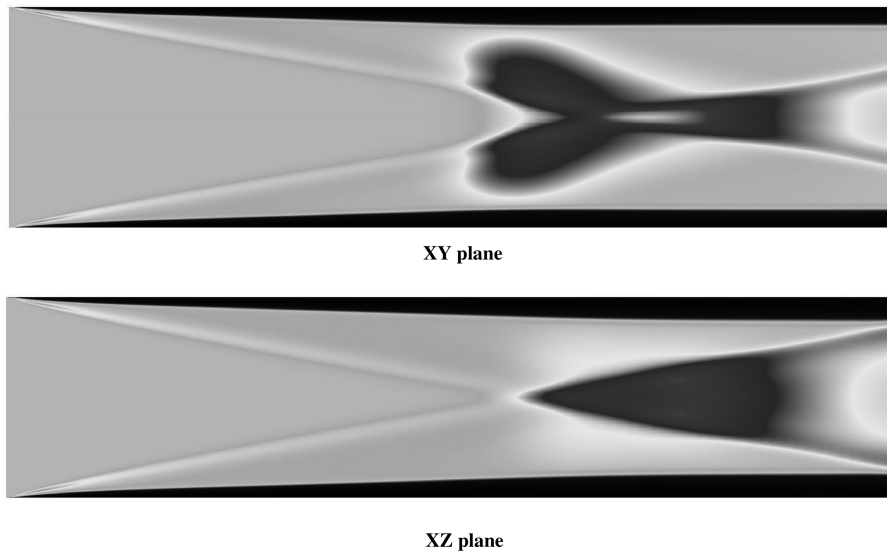
XY plane

XZ plane

Fig. 4 Top and side view of density contours on the central plane of the inlet, $M_\infty = 5.15$, Rey $= 1.64 \times 10^5$.
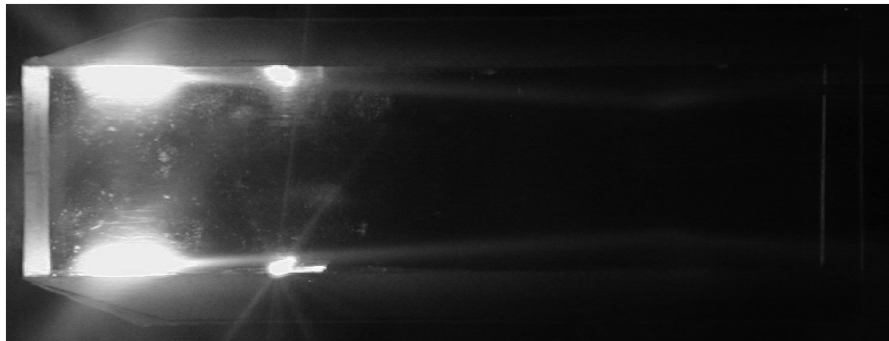

Fig. 5 Discharge along inlet vertical sidewalls, side-by-side electrode configuration, $E = 650$ V, $I = 40$ mA.

shock angle originating from the vertical leading edges of the inlet. As a consequence, the shock intersection points move upstream, and most important, the overall static pressure distribution at the exit plane of the inlet is higher than when the dc discharge is deactivated.

The drift–diffusion plasma model generates the most accurate ion number density contours under a similar test condition [21,22]. In Fig. 6, the ion number density of the side-by-side dc discharge is seen to concentrate mostly over the cathodes where the Joule heating also reaches its maximum. The maximum ion number density concentration has attained a value of $8.8 \times 10^{11}/\text{cm}^3$, which agrees reasonably well with experimental measurement [12]. A trace amount of the charged particles is also conveyed downstream. In short, Joule and electrode heating are the key elements of the electromagnetic perturbation and are introduced in the innermost region of the shear layer. Simplified plasma models with heat

addition can reproduce these physical phenomena and provide a reasonable description of the dc discharge for MFD interactions [16,17].

The fundamental mechanism of the MFD compression is built on the concept that a small electromagnetic perturbation to the displacement thickness of the shear layer is amplified by the viscous–inviscid interaction, which generates a higher pressure plateau [15,16]. Therefore the MFD compression does not drastically alter the basic flowfield structure but produces stronger oblique shocks from the discharging electrodes within the inlet. This fact is substantiated by both experimental observations and computational results [16].

A comparison of the Pitot pressure survey and the computed results using the fine-mesh system is depicted in Fig. 7. The data are collected at the streamwise station of $x/L = 0.75$, and the activated
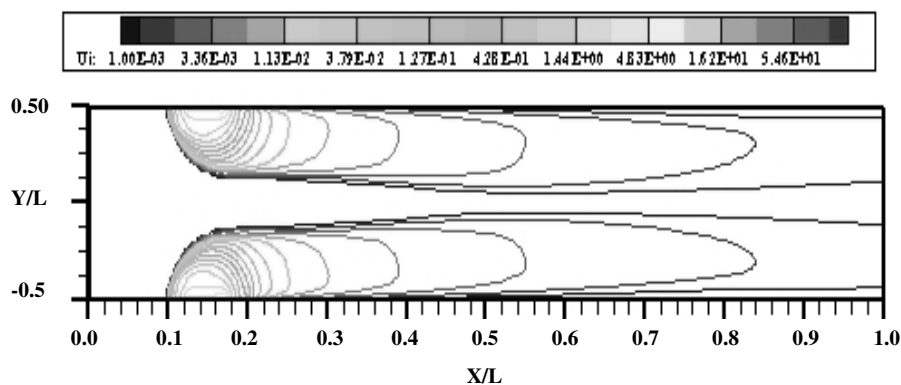

Fig. 6 Ion number density contours of a typical side-by-side dc discharge arrangement, $V = 1.0$ kV, $\rho = 8.26 \times 10^{-6}$ g/cm^3.
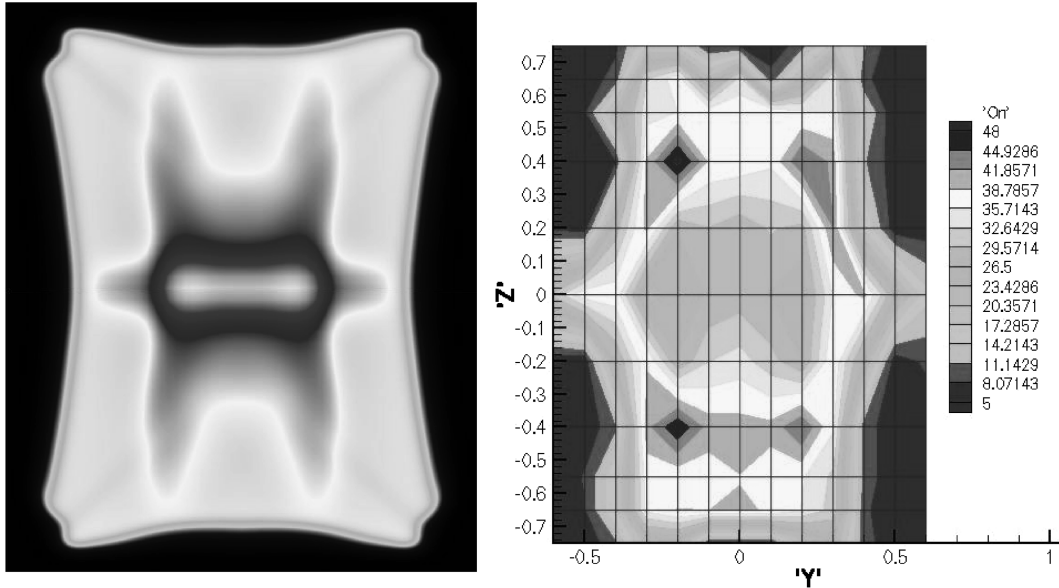
Fig. 7   Comparison of Pitot pressure contours with actuated dc discharge, $M_\infty = 5.15$, Rey $= 1.64 \times 10^5$, $E = 650$ V, $I = 40$ mA.

dc discharge is across the vertical sidewalls. The data were collected for the stagnation pressure of 370 torr (2.71 kPa). At this streamwise location, the oblique shocks originating from the sidewall leading edges parallel to the z coordinate have already intersected and diverted from each other, showing a wide domain of lower Pitot pressure over the y coordinate. Because there is a vast difference in data point density between the experiment and computation (400 vs 5985), the comparative study must be limited to a qualitative nature [25]. In addition, the experimental and computational results are prepared using different graphic packages; thus a one-to-one comparison is not achievable. Despite different scales of color for contour levels, the data and computed results indicate an inviscid core still exists at this cross-section plane. Both results show the Pitot pressure retaining a value near 20.4 torr (unperturbed freestream value). The computed results also show that the shear layer thickens in the corner and at the middle points of the sidewalls. Experimental data are absent in this region because the size of the Pitot probe (OD $= 0.159$ cm) prevents all near-wall measurements. Nevertheless, the basic shock wave structures are identical, and the magnitude of the measured and computed Pitot pressures agrees reasonably well.

Figure 8 presents the computed temperature profiles in x–y plane over the centerline of the cathode, $x/L = 0.124$ and near the inlet exit, $x/L = 0.875$. In this presentation, the actuated dc discharge and the unperturbed simulations are grouped together accentuating the thermal perturbation to the flowfield by the surface gas discharge. The numerical simulation captures the physics in that the Joule heating and the convective electrode heating release a significant amount of thermal energy into the airstream. The elevated temperature in the inner region of the shear layer reduces the value of density locally, and in turn significantly increases the displacement thickness of the shear layer. In addition, the total Joule heating over the cathode is on the same order of magnitude as the convective electrode heating, 7.4 vs 6.6 W; whereas the magnitude of the computed electrostatic force is merely 430 dyne/cm^3 and this force is exerted mostly downward toward the cathode. In a shear layer over flat surface, this force is not supported by the shear stress and is directly transmitted to the solid surface. Therefore the computed result substantiates the fact that the thermal effect of the dc discharge is dominant over that of the electrostatic force for the ensuing viscous–inviscid interaction.

Far downstream to the discharging electrodes, the Joule heating diminishes and the convective heat transfer persists. The energy dissipating shear layer actually heats the model surface to reveal a higher model surface temperature. Despite the high electron temperature, the nonequilibrium ion temperature is still retained at
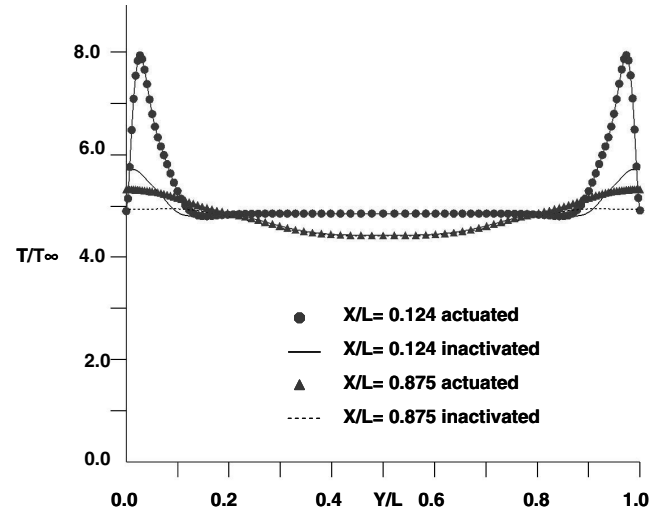

Fig. 8   Comparison of temperature profiles with the rectangular inlet, $M_\infty = 5.15$, Rey $= 2.57 \times 10^5$, $E = 800$ V, $I = 80$ mA.

the energy state of ambient condition [30]. From experimental measurement, the vibration temperature is around 5000 k and is the result of energy cascading from the ionization [12,13,15,16]. From the viewpoint of plasma generation, this behavior is extremely important but the vibrational internal degree of freedom contributes very little to the interacting flowfield structure.

The computed Pitot pressure distributions in the x–y plane for three selected streamwise locations of $x/L = 0.20, 0.75$, and 1.0 are given in Fig. 9. All the following numerical simulations are generated at the higher stagnation pressure of 580 torr. The results obtained with activated dc discharge are designated by the red symbols and lines under the otherwise identical flow condition. The computed results fully substantiate the fact that the dc discharge indeed is a small electromagnetic perturbation to the viscous–inviscid interaction. When the dc discharge is activated, the oblique shocks that originate from the leading edge intensify by a steepened oblique shock angle. Downstream from the shocks' intersection, the Pitot pressure results generally indicate a higher level at the wave front than the unperturbed counterpart. The shock waves are clustered toward the middle of the rectangular inlet. However the basic flowfield structure remains unaltered.

Figure 10 depicts a comparison of experimental and computed Pitot pressures along the centerline of the rectangular inlet when the
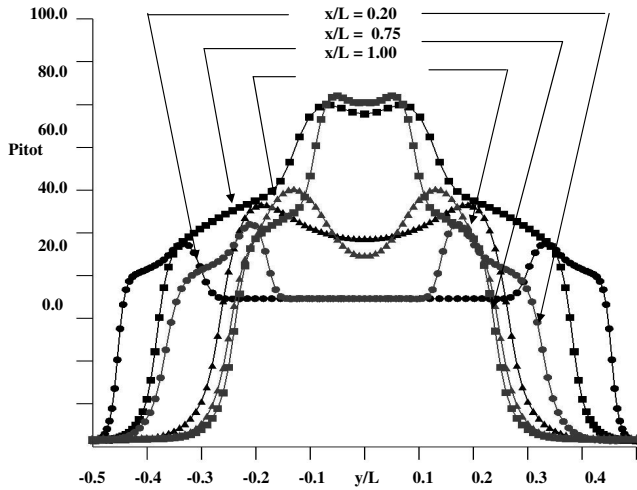
Fig. 9 Computed Pitot pressure profiles at three streamwise locations, $M_\infty = 5.15$, Rey $= 2.57 \times 10^5$, $E = 800$ V, $I = 80$ mA.

Fig. 11 Comparison of Pitot pressure profiles at $x/L = 0.6$, $M_\infty = 5.15$, Rey $= 2.57 \times 10^5$, $E = 775$ V, $I = 80$ mA.

dc discharge is either actuated or deactivated. Both results, generated at the stagnation pressure of 580 torr, capture the interacting oblique shocks within the inlet [25]. When the dc discharge is actuated, the induced oblique shock becomes steeper and moves the incipient point of the shock waves upstream. The ensured expansion behind the strengthened shock and a lower static pressure along the centerline produce a lower Pitot pressure downstream. The actuated dc discharge leads to a higher peak Pitot pressure and an upstream movement, in contrast to its deactivated counterpart. The computed results reach very good agreement with the experimental observations. The computations underpredict the peak Pitot pressure by 2% and overpredict the uniform entrance condition by 1.2%. This small discrepancy in magnitude is directly attributable to the fluctuation of the dc discharge and the uncertain Mach number at the entrance of the inlet due to model blockage.

Additional verification of the MFD interacting phenomenon is obtained by comparing the computed Pitot pressure profiles between the intersections of oblique shocks and the exit of the rectangular inlet. Figure 11 presents a comparison of the normalized Pitot pressure profiles and data at the streamwise location of $x/L = 0.6$, along the line at the middle point of the z coordinate and halfway between the middle point and the upper wall. The data were collected at a stagnation pressure of 580 torr; thus the referenced freestream Pitot pressure had a value of 30 torr [25]. The Pitot pressure is generated under a dc discharge of a total current of 80 mA with an applied electric field of 755 V. Because the dc discharge is operated
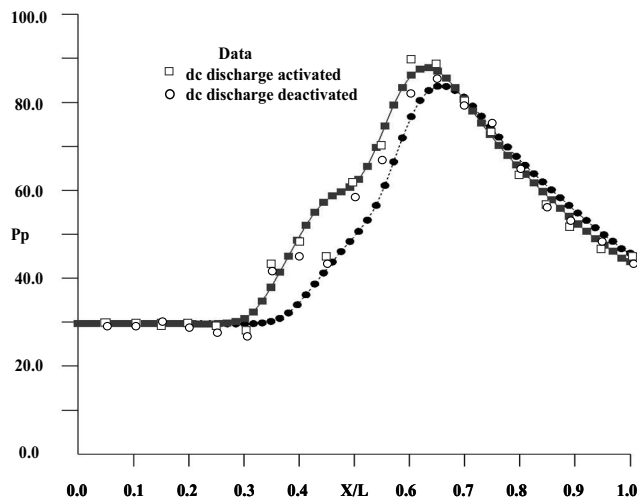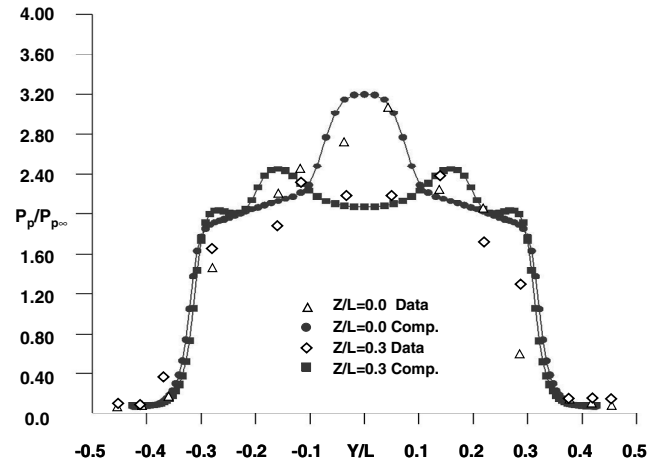
in the abnormal discharge regime, the data are averaged values for the duration of 1.5 s of data acquisition. The data scattering band has a magnitude of 4.8%. Nevertheless, the computed results reach a reasonable agreement with the data. Most important, the computations in the central plane of the z coordinate capture the shock-on-shock interaction and agree with experimental observation.

A comparison of the Pitot pressure profiles near the inlet exit plane is given in Fig. 12. Again, the Pitot pressure profiles are presented along the y coordinate at different values of the z coordinate. Although the dc discharge is operated at nearly the identical condition, the behavior of the Pitot pressure is opposite to that at the upstream plane because the oblique shocks are now diverging from each other. The profile at the middle section of the inlet is lower than the sidewall region. The computed results duplicate the basic interacting flowfield structure in boundary-layer thickness and shock fronts, but computations reach only a marginally acceptable agreement with the data. These rather large discrepancies between the data and the computations exceed a value of 4.8% at the shocks. The major contributor of this disparity may be the unstable dc discharge pattern that leads to the oscillating shock front [25]. The Pitot probe may be alternatively sampled the flow data upstream and downstream of the oblique shocks.

VI. Magnetofluid-Dynamic Compression

The performance of an inlet is measured by the compression in static pressure and loss in the stagnation pressure [1,2]. The data from the small model installed in the hypersonic plasma channel are
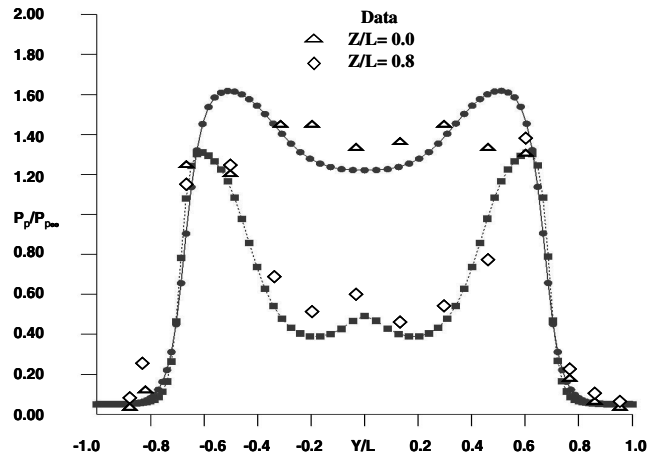

Fig. 10 Compared Pitot pressure distributions, $M_\infty = 5.15$, Rey $= 2.57 \times 10^5$, $E = 775$ V, $I = 80$ mA.

Fig. 12 Comparison of Pitot profiles near the inlet exit, $x/L = 0.95$, $M_\infty = 5.15$, Rey $= 2.57 \times 10^5$, $E = 775$ V, $I = 80$ mA.

dc discharge actuated
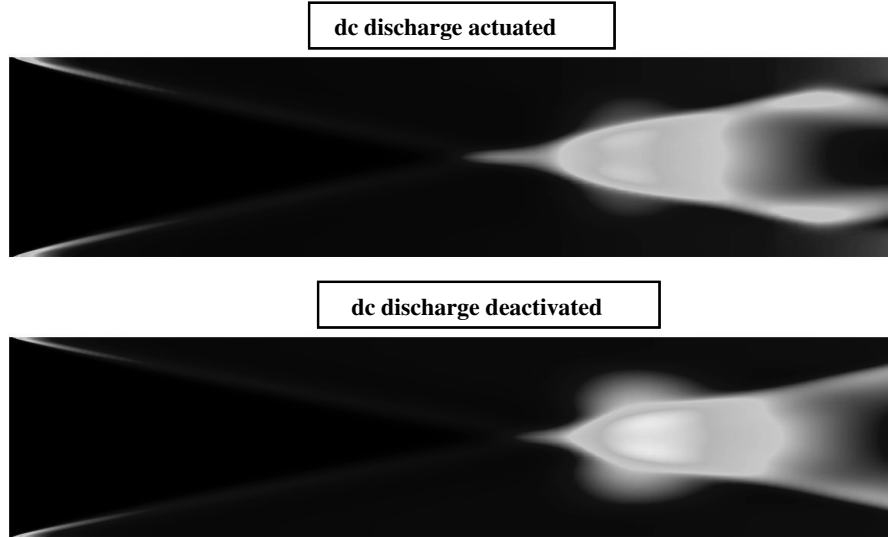

dc discharge deactivated

Fig. 13 Static pressure comparison with actuated and deactivated dc discharge, $E = 800$ V, $I = 80$ mA.

limited to only the Pitot pressure measurements; therefore the computational simulation plays a pivotal role in interpreting the experimental finding. Based on the result of comparison with experimental data, the maximum calibrated error of the computational simulation is 4.8%.

For the experimental investigation, the power input to the plasma is limited to 64 W ($E = 800$ V and $I = 80$ mA); therefore the effect of the magnetoaerodynamic compression is small. As anticipated, the difference between data of an actuated and deactivated dc discharge is only pronounced at the shock intersections [22,25]. This behavior is also clearly revealed in the computed static pressure contours with actuated and deactivated dc discharge, as shown in Fig. 13. When the dc discharge is activated, the induced oblique shocks from the electrode embedded sidewall gain strength. These shocks have a steeper shock angle and intersect each other upstream compared with the flow without electromagnetic perturbation. The pair of perpendicular oblique shocks originating from the dielectric top and bottom walls retain the same slope, and the intersection point remains unaltered.

Figure 14 depicts the difference in static pressure distributions along the centerline and horizontal sidewall of the rectangular inlet with and without the activated dc discharge. All the computed static pressures are normalized with respect to the freestream value of 0.93 torr. The dc discharge strengthens the oblique shock emerging from the leading edge and moves the shock intersection point upstream. The peak value of the static pressure of the shock-on-shock interacting zone increases by 12.1%. An inflecting point of the pressure plateau also appears in the pressure distribution along the
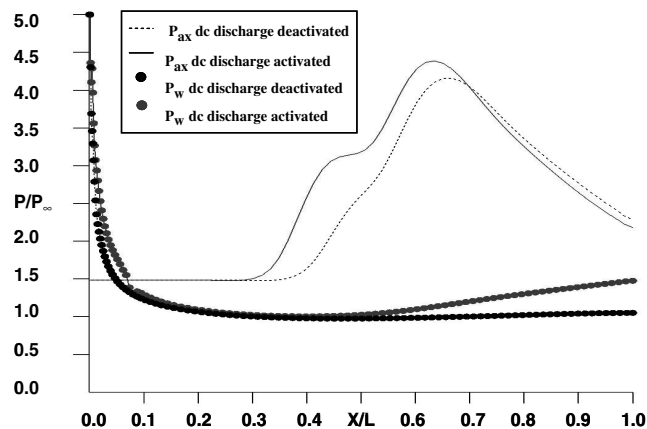
centerline of the inlet, a characteristic of static pressure behavior of shock impingement on a boundary layer [33]. The pressure along the centerline also expands more rapidly from the peak value than the unperturbed flow toward downstream. The surface pressure distributions have a different behavior from the core flow of the inlet. The differences in surface pressure are pronounced at the electrode near the leading edge as is a stronger and continued compression when the dc discharge is activated. The maximum difference occurs at the exit of the inlet, and the magnitude exceeds 14.2%.

The overall effect of MFD compression on the static pressure distributions is depicted in Fig. 15. In this presentation, three selected static pressure distributions in the crossflow plane at the streamwise locations of $x/L = 0.2$, 0.75, and 1.0 are given. All static pressure distributions show that when the dc discharge is actuated, the oblique shock is strengthened. The shock wave intersection moves upstream and elevates the overall static pressure to a higher value. The pattern of static pressure distributions bears a strong resemblance to the Pitot pressure in Fig. 9. However there is a critical difference in the sidewall region within the boundary layer: the shear dominant region is unable to support a pressure gradient across the layer. After the dc discharge intensifies the viscous–inviscid interaction, the static pressure is consistently higher than the unperturbed counterpart. This elevated static pressure in the near sidewall region becomes a significant contributor to the magnetofluid-dynamic compression.
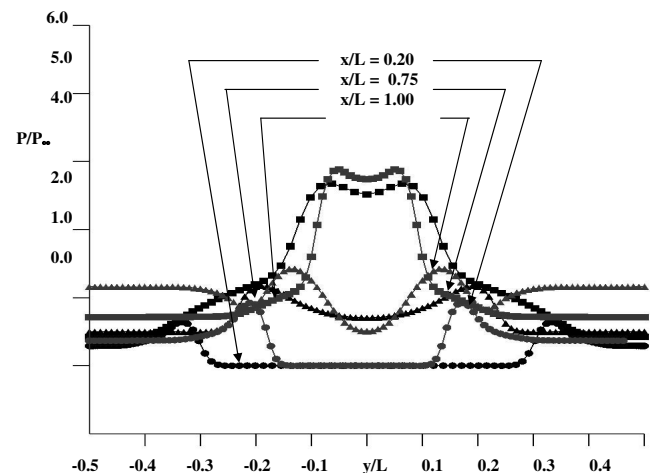

Fig. 14 Static pressure distributions along the inlet, $M_\infty = 5.15$, Rey $= 2.57 \times 10^5$, $E = 775$ V, $I = 80$ mA.

Fig. 15 Static pressure behavior with and without dc discharge at different streamwise locations, $M_\infty = 5.15$, Rey $= 2.57 \times 10^5$, $E = 775$ V, $I = 80$ mA.
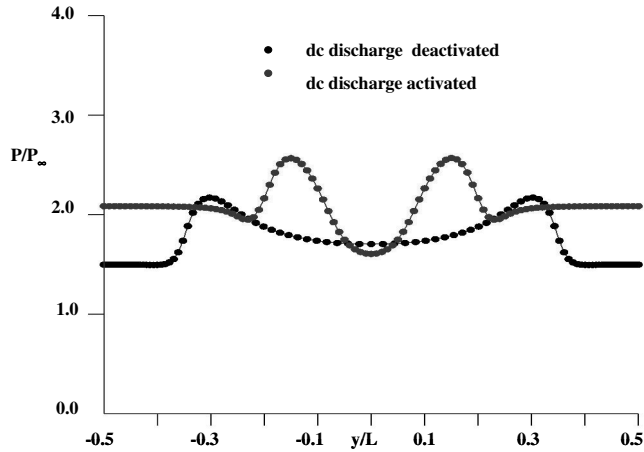
Fig. 16 Static pressure profiles in x–y plane near inlet exit with/without dc discharge, $M_\infty = 5.15$, Rey $= 2.57 \times 10^5$, $E = 775$ V, $I = 80$ mA.

The computed static pressure distributions in the x–y plane and near the inlet exit ($x/L = 0.95$) are given in Fig. 16. The rise and fall of the pressure near the plane of symmetry reveals the strengthened pressure interaction phenomenon. The static pressure distribution attains a nearly constant inner core when the dc discharge is deactivated. However this behavior changes when the dc discharge is actuated; the static pressure rises from the intersections of the oblique shocks. In addition, the static pressure in the viscous dominated region is also consistently higher than the unperturbed flow, showing an additional side compression derived from the electromagnetic perturbation in the entrance region of the inlet.

Figure 17 presents a comparison of the computed static pressure distributions in the x–z plane near the inlet exit. The difference in pressure distributions with and without the activated dc discharge is similar to that in the x–y plane, except the pressure level is consistently higher by the induced vertical sidewall compression over most of the inner core region. Because the electrodes are embedded only in the vertical sidewalls, there is no additional compression from the horizontal surfaces. The increased static pressure is the result of the MFD interaction originating in the entrance region of the inlet.

The averaged static pressure over the entire exit cross section is 11.7% greater than the counterpart without electromagnetic perturbation. This additional compression is attained using less than 64 W of total power input for plasma generation. The investigated MFD compression is not optimized, because the final compression at the inlet exhibits a significant dependence in electrode arrangement and placement. At a higher Mach number or using a series electrodes configuration, the MFD compression is anticipated to improve the effectiveness of the virtual variable geometry cowl. Nevertheless, the concept of using an electro-
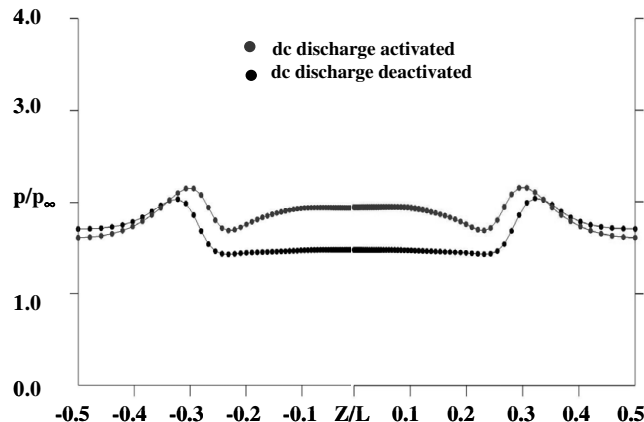

Fig. 17 Static pressure profiles in x–z plane near inlet exit with/without dc discharge, $M_\infty = 5.15$, Rey $= 2.57 \times 10^5$, $E = 775$ V, $I = 80$ mA.
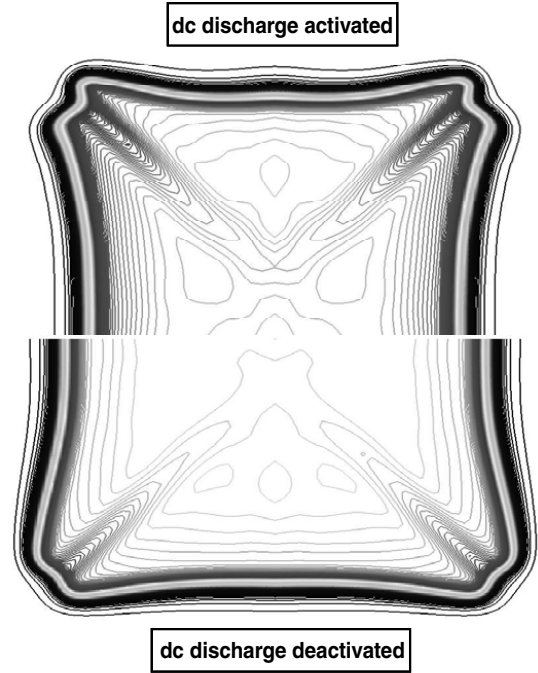

Fig. 18 Stagnation pressure contours at inlet exit, $M_\infty = 5.15$, Rey $= 2.57 \times 10^5$, $E = 775$ V, $I = 80$ mA.

magnetic perturbation to enhance the pressure interaction for a magnetofluid-dynamic inlet compression has been demonstrated. The compression ratio is rather modest at a low power input, with only the two sidewalls having a dc discharge. The total compression can be doubled through implementation of a dc discharge on all four inlet surfaces. From the ensuing experimental effort for magnetofluid-dynamic compression to emulate a variable geometry cowl, the MFD compression is found to be dependent on the electrode size and placement. Continued research is presently being sustained to search for an optimal electrode arrangement.

Another important aspect of the inlet performance is the loss of stagnation pressure by the shock compression process, which is an unavoidable consequence in supersonic flow. Figure 18 depicts a direct comparison of the normalized stagnation pressure contours between the activated and deactivated dc discharge near the inlet exit ($x/L = 0.95$). The levels of contours and the computational cross sections are identical between the computed results. In theory, the change of entropy is proportional to the third power of the shock strength and hence the flow deflection angle of oblique shocks. The lost of stagnation pressure of the inner core flow is negligible but incurs only from the reduced core size through the magneto side compression. A similar pattern shall be anticipated from a mechanical compression ramp. However the loss can be substantially reduced by a multiple electrodes arrangement that is not easily achievable by mechanical devices.

According to the classic pressure interaction theory [23], the intensity of the MFD compression strongly depends on the freestream Mach number. If the electromagnetic perturbation can be maintained at a higher Mach number, the effectiveness of MFD compression to emulate a variable geometry cowl would greatly increase. A preliminary computing simulation presented in Fig. 19 seems to substantiate this fact. Numerical simulations under the identical dc discharge condition of 80 mA and 800 V, but at a higher Mach number of six, are performed. The computed results show a greater compression; however the full potential of MFD compression cannot be realized without an optimum electrode arrangement.

VII.   Conclusions

A viable application of plasma actuators for flow control in the hypersonic regime has been simulated by computational analysis
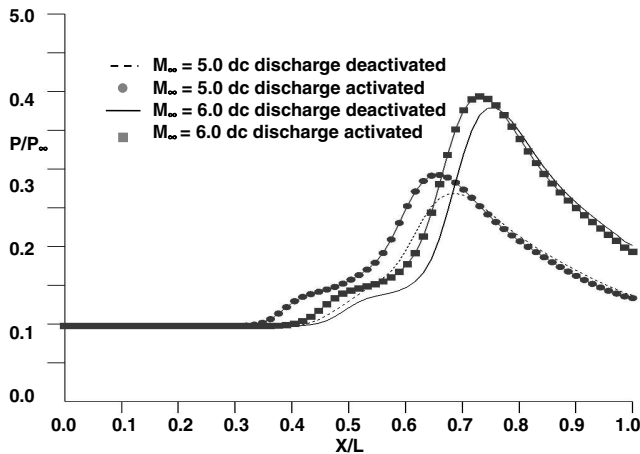
Fig. 19 Effect of Mach number to MFD interaction, Rey = 2.57×10^5, $E = 800$ V, $I = 80$ mA.

using the magnetofluid-dynamic equation in the low magnetic Reynolds number limit with plasma models. The key mechanism of an effective plasma actuator for flow control is the amplification of an electromagnetic perturbation by the unique hypersonic, viscous–inviscid interaction. The basic approach introduces a direct current discharge near the sharp leading edges of the inlet, thereby altering the slope of the surface shear-layer thickness, resulting in a stronger viscous–inviscid interaction. The numerical results are first validated by comparing with experimental Pitot pressure measurements of the flowfield. Then the shock–shock and shock–boundary-layer interactions are analyzed within the constant cross-section rectangular inlet that emulates a variable geometry cowl. For a dc discharge maintained by an electric potential of 800 V and an electrical current of 80 mA over the total discharge surface area of 8.13 cm^2, the magnetofluid-dynamic interaction generated 11.7% greater compression at the inlet exit than the unperturbed flow.

The magnetofluid-dynamic compression performs as a virtual cowl that enhances performance of the constant cross-section inlet and can produce significant weight savings through a much simpler flow control mechanism. At the freestream Mach number of 5.15, the magnetofluid-dynamic sidewall compression produces an 11.7% gain using a power input of 7.87 W per square centimeter of electrode surface area for plasma generation. In application, this power scaling law of the plasma actuator holds equally well for a virtual hypersonic leading strake. In this aspect, the present approach using a plasma actuator for hypersonic flow control has overcome the fundamental inefficient ionization process.

The numerical results also show that effectiveness of the virtual variable geometry cowl can increase with higher freestream Mach numbers, if the intensity of the dc discharge can be sustained. Precise and optimal electrode placement in the inlet becomes pivotal for a wide range of versatile practical applications. Research efforts in this area are presently continuing.

Acknowledgments

References

[1] Murthy, S. N. B., and Curran, E. T., *High Speed Flight Propulsion Systems*, Progress in Aeronautics and Astronautics, AIAA, New York, 1991.

[2] Kurth, G., *Critical Physical Phenomena in Scramjet Propulsion*, CP-600, AGARD, 2002, pp. C5.1–C5.11.

[3] Dolling, D. S., "Fifty Years of Shock-Wave/Boundary-Layer Interaction Research: What Next?," *AIAA Journal*, Vol. 39, No. 8, 2001, pp. 1517–1531.

[4] Peake, D., and Tobak, M., "Three-Dimensional Interactions and Vortical Flows with Emphasis on High Speed," NASA TM 81169, March 1980.

[5] Andreopoulos, Y., Agui, J. H., and Briassulis, G., "Shock Wave–Turbulence Interaction," *Annual Review of Fluid Mechanics*, Vol. 32, 2000, pp. 309–345.

[6] Resler, E. L., and Sears, W. R., "The Prospect for Magneto-Aerodynamics," *Journal of the Aeronautical Sciences*, Vol. 25, April 1958, pp. 235–245, 258.

[7] Chernyi, G. G., "Some Recent Results in Aerodynamic Applications of Flow with Localized Energy Addition," AIAA Paper 99-4819, Norfolk VA, Nov. 1999.

[8] Bityurin, V., Kilmov, A., Leonov, S., Lutsky, A., Van Wie, D., Brovkin, V., and Kolesnichenko, Yu., "Effect of Heterogeneous Discharge Plasma on Shock Wave Structure and Propagation," AIAA Paper 99-4940, Norfolk, VA, Nov. 1999.

[9] Leonov, S. B., Yarantsev, D. A., Gromov, V. G., and Kuriachy, A. P., "Mechanisms of Flow Control by Near-Surface Electrical Discharge Generation," AIAA Paper 2005-0780, Jan. 2005.

[10] Shneider, M. N., and Macheret, S. O., "Hypersonic Aerodynamic Control and Thrust Vectoring by Nonequilibrium Cold-Air MHD Devices," AIAA Paper 2005-0979, Reno, NV, Jan. 2005.

[11] Leonov, S., Bityurin, V., Savelkin, K., and Yarantsev, D., "Effect of Electrical Discharge on Separation Processes and Shock Position in Supersonic Airflow," AIAA Paper 2002-0355, Reno, NV, Jan. 2002.

[12] Menart, J. Shang, J. S., Kimmel, R., and Hayes, J., "Effects of Magnetic Fields on Plasma Discharges at Mach 5 Wind Tunnel," AIAA Paper 2003-4165, Reno, NV, Jan. 2004.

[13] Kimmel, R., Hayes, J., Menart, J., and Shang, J. S., "Effect of Magnetic Filed on Surface Plasma Discharges at Mach 5," *Journal of Spacecraft and Rockets*, Vol. 43, No. 6, 2006, pp. 1340–1346.

[14] Bityurin, V. A., Bocharov, A. N., and Lineberry, J. T., "Results of Experiments on MHD Hypersonic Flow Control," AIAA Paper 2004-2263, Portland, OR, June 2004.

[15] Shang, J. S., and Surzhikov, S. T., "Magnetoaerodynamic Actuator for Hypersonic Flow Control," *AIAA Journal*, Vol. 43, No. 8, Aug. 2005, pp. 1633–1643.

[16] Shang, J. S., Surzhikov, S. T., Kimmel, R., Gaitonde, D., Menart, J., and Hayes, J., "Mechanisms of Plasma Actuators for Hypersonic Flow Control," *Progress in Aerospace Sciences*, Vol. 41, No. 8, Nov. 2005, pp. 642–668.

[17] Updike, G., Shang, J. S., and Gaitonde, D. V., "Hypersonic Separated Flow Control Using Magneto-Aerodynamic Interaction," AIAA Paper 2005-0164, Reno, NV, Jan. 2005.

[18] Poggie, J., "Computational Studies of High-Speed Flow Control with Weakly Ionized Plasma," AIAA Paper 2005-0784, Reno, NV, Jan. 2005.

[19] Gaitonde, D. V., "Simulation of Local and Global High-Speed Flow Control with Magnetic Field," AIAA Paper 2005-0560, Reno, NV, Jan. 2005.

[20] Borghi, C., Carraro, M., and Cristofolini, A., "Axisymmetric Hall Configuration for the MHD Interaction in Hypersonic Flows," AIAA Paper 2005-4785, Toronto, Canada, June 2005.

[21] Surzhikov, S. T., and Shang, J. S., "The Hypersonic Quasineutral Gas Discharge Plasma in a Magnetic Field," *Proceedings of the Third MIT Conference on Computational Fluid and Solid Mechanics*, MIT Press, Boston, 2005, pp. 1004–1005.

[22] Surzhikov, S. T., and Shang, J. S., "Two-Component Plasma Model for Two-Dimensional Glow Discharge in Magnetic Field," *Journal of Computational Physics*, Vol. 199, No. 2, Sept. 2004, pp. 437–464.

[23] Hayes, W. D., and Probstein, R. F., *Hypersonic Flow Theory*, Academic Press, New York, 1959.

[24] Shang, J. S., "Electromagnetic Perturbation to Hypersonic Viscous–Inviscid Interactions," AIAA Paper 2006-0709, Reno, NV, Jan. 2006.

[25] Shang, J. S., Menart, J., Kimmel, R., and Hayes, J., "Magneto-Fluid-Dynamics Hypersonic Compression Inlet," AIAA Paper 2006-0764, Reno, NV, Jan. 2006.

[26] Mitchner, M., and Kruger, C. H., Jr., *Partially Ionized Gases*, Wiley, New York, 1973, pp. 188–198.

[27] Sutton, G. W., and Sherman, A., *Engineering Magnetohydrodynamics*, McGraw–Hill, New York, 1965, pp. 295–308.

[28] Boeuf, J. P., and Pitchford, L. C., "Electrodrodynamic Force and Aerodynamic Flow Acceleration in Surface Dielectric Barrier Discharge," *Journal of Applied Physics*, Vol. 97, No. 103307, 2005, pp. 103307-1, 103307-10.

[29] Shang, J. S., "Electromagnetic Field of Dielectric Barrier Discharge," AIAA Paper 2005-5182, Toronto, CA, June 2005.

[30] Raizer, Yu. P., *Gas Discharge Physics*, Springer–Verlag, Berlin, 1991.

[31] Rumsey, C., Biedron, R., and Thomas, J., "CFL3D: Its History and Some Recent Applications," NASA TM-112861, May 2007.

[32] Thomas, J. L., Diskin, B., and Brandt, A., "Textbook Multigrid Efficiency for Fluid Simulation," *Annual Review of Fluid Mechanics*, Vol. 35, Jan. 2003, pp. 317–340.

[33] Shang, J. S., and Hankey, W. L., "Numerical Solution of the Navier–Stokes Equations for a Three-Dimensional Corner," *AIAA Journal*, Vol. 15, No. 11, 1977, pp. 1675–1582.

X. Zhong
Associate Editor